Charge density wave activated excitons in TiSe$_2$–MoSe$_2$ heterostructures ⓕ

ⓘD Jaydeep Joshi, ⓘD Benedikt Scharf, ⓘD Igor Mazin, et al.

COLLECTIONS

Note: This paper is part of the Special Topic on Light and Matter Interactions.

ⓕ   This paper was selected as Featured

View Online   Export Citation   CrossMark

Charge density wave activated excitons in TiSe$_2$–MoSe$_2$ heterostructures $_\text{F}$

Jaydeep Joshi,[1,2] (ID) **Benedikt Scharf,**[3] (ID) **Igor Mazin,**[1,2] (ID) **Sergiy Krylyuk,**[4] (ID) **Daniel J. Campbell,**[5] (ID)
Johnpierre Paglione,[5,6] (ID) **Albert Davydov,**[2,4,5] (ID) **Igor Žutić,**[7] (ID) **and Patrick M. Vora**[1,2,a)] (ID)

AFFILIATIONS

[1] Department of Physics and Astronomy, George Mason University, Fairfax, Virginia 22030, USA
[2] Quantum Science and Engineering Center, George Mason University, Fairfax, Virginia 22030, USA
[3] Institute for Theoretical Physics and Astrophysics and Würzburg-Dresden Cluster of Excellence ct.qmats,
   University of Würzburg, Am Hubland, 97074 Würzburg, Germany
[4] Materials Science and Engineering Division, National Institute of Standards and Technology, Gaithersburg,
   Maryland 20899, USA
[5] Maryland Quantum Materials Center, Department of Physics, University of Maryland, College Park, Maryland 20742, USA
[6] Canadian Institute for Advanced Research, Toronto, Ontario M5G 1Z8, Canada
[7] Department of Physics, University at Buffalo, Buffalo, New York 14260, USA

Note: This paper is part of the Special Topic on Light and Matter Interactions.
[a)] Author to whom correspondence should be addressed: pvora@gmu.edu

ABSTRACT

Layered materials enable the assembly of a new class of heterostructures where lattice-matching is no longer a requirement. Interfaces in these heterostructures therefore become a fertile ground for unexplored physics as dissimilar phenomena can be coupled via proximity effects. In this article, we identify an unexpected photoluminescence (PL) peak when MoSe$_2$ interacts with TiSe$_2$. A series of temperature-dependent and spatially resolved PL measurements reveal that this peak is unique to the TiSe$_2$–MoSe$_2$ interface, is higher in energy compared to the neutral exciton, and exhibits exciton-like characteristics. The feature disappears at the TiSe$_2$ charge density wave transition, suggesting that the density wave plays an important role in the formation of this new exciton. We present several plausible scenarios regarding the origin of this peak that individually capture some aspects of our observations but cannot fully explain this feature. These results therefore represent a fresh challenge for the theoretical community and provide a fascinating way to engineer excitons through interactions with charge density waves.

I. INTRODUCTION

Two-dimensional (2D) material interfaces in van der Waals (vdW) heterostructures provide a fascinating playground to explore proximity effects.[1] The relaxation of lattice constraints on heterostructure assembly allows for the arbitrary stacking of 2D materials.[2] These interfaces may, in some cases, support emergent states absent from the parent compounds, with superconductivity in twisted bilayer graphene and moiré excitons in transition metal dichalcogenides (TMDs) serving as remarkable examples.[3–6] Many studies of vdW heterostructures incorporate semiconducting TMDs

as an active component. This commonality is due to the availability of high-quality samples, well-established exfoliation procedures,[7,8] and the existence of tightly bound 2D excitons.[9]

The zoology of excitons in monolayer (ML) semiconductors is vast: Neutral (X^0) and charged excitons or trions (X^- or X^+),[9–12] neutral and charged biexcitons,[13–16] and dark exciton states[17–20] have all been observed and exhaustively studied in semiconducting TMDs. The 2D nature of TMD excitons also renders them highly sensitive to the local dielectric environment,[21–26] allowing for a remote, contact-free probe of interface characteristics in vdW

heterostructures. For instance, semiconductor hetero-bilayer and homo-bilayer heterostructures exhibit new photoluminescence (PL) emission peaks from interlayer excitons and splitting of exciton peaks due to the moiré potential.[5,27–30] Proximity effects between 2D magnets and semiconductors lead to large valley splittings,[31,32] and magnetic manipulation of exciton PL energy, intensity, and selection rules.[1,33–35] Exotic correlated insulating states such as Wigner crystals and Mott insulators in twisted TMD semiconductor heterostructures are also observable in PL spectra.[36–38] However, there have been no studies exploring the impact of similar electron correlated phases such as charge density waves (CDWs)[39] on PL in vdW heterostructures.

Here, we investigate optical signatures of interlayer coupling between the semiconductor $MoSe_2$ and the putative excitonic insulator 1T-$TiSe_2$,[40–43] which hosts a commensurate $2 \times 2 \times 2$ CDW state below 200 K. We find that the CDW alters the manifold of optically active excitons at the $TiSe_2$–$MoSe_2$ interface, which results in a new PL peak above X^0. This feature, referred to as H1, appears in the $MoSe_2$ PL spectrum with a linewidth comparable to X^0. While lower-energy PL sidebands are relatively common in TMDs due to phonon replicas and exciton localization,[44–48] these observations are the first such detection of a higher-energy PL sideband. Detailed temperature-dependent, power-dependent, and spatially resolved

PL measurements on multiple heterostructures demonstrate that H1 has an origin consistent with a native exciton state rather than a localized exciton or defect state. However, H1 disappears at the $TiSe_2$ CDW temperature, which suggests that these two phenomena are closely linked. We have identified multiple plausible scenarios and discuss them in detail, although none are able to explain all aspects of our observations. Interactions between excitons and CDWs provide a fresh challenge to the theoretical community and a novel method for engineering excitons in 2D materials.

II. RESULTS

A. Optical characterization of vdW heterostructures

The optical microscope images of two $TiSe_2$–$MoSe_2$ vdW heterostructures termed sample 1 and sample 2, respectively, are presented in Figs. 1(a) and 1(b). These samples are assembled by a modified viscoelastic method[49] that incorporates atomic force microscope (AFM) cleaning.[50] The black dashed line outlines the ML–$MoSe_2$ flake in each sample. Representative low-temperature (5 K) PL spectra taken on (black) and off (red) the interface are shown in Figs. 1(c) and 1(d) for the two samples. Emission from the $MoSe_2$ X^- ($\approx$1.62 eV) and X^0 ($\approx$1.65 eV) states agrees with prior observations in both energy and linewidth.[11,18,51–53] The interface PL
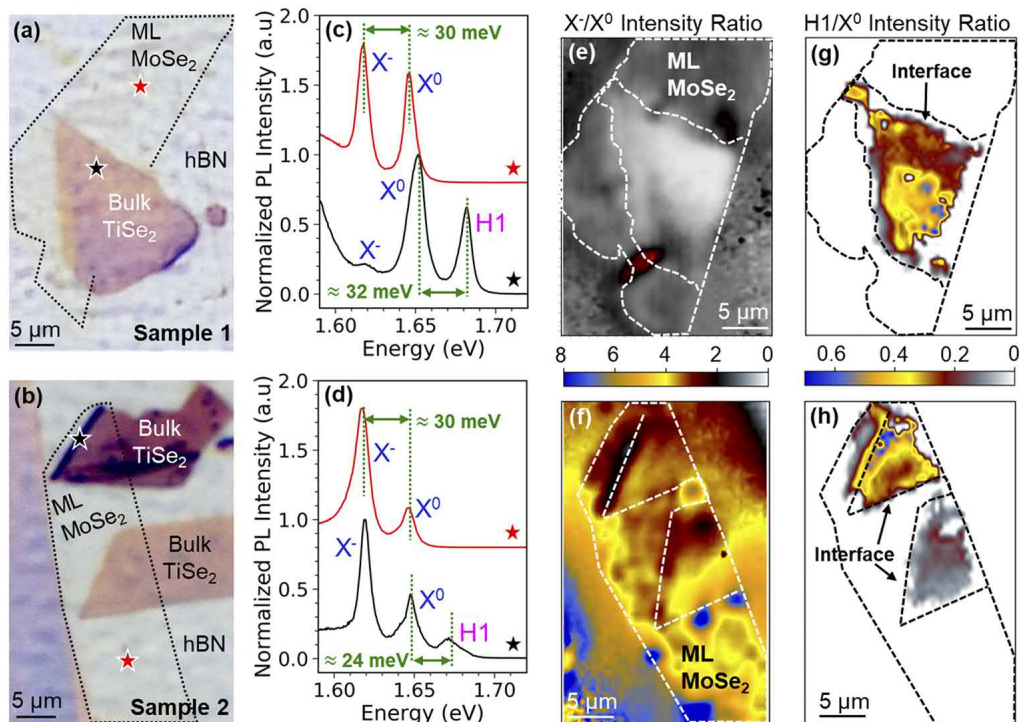
FIG. 1. Optical microscope images of $TiSe_2$–$MoSe_2$ vdW heterostructures: (a) sample 1 and (b) sample 2. The black dotted line outlines the ML–$MoSe_2$ layer. 5 K PL spectra taken on (black) and off (red) the interface for (c) sample 1 and (d) sample 2. These locations are denoted by red and black stars in panels (a) and (b), respectively. In addition to the X^0 and X^- emission observed in ML–$MoSe_2$, the H1 PL peak appears at $\approx$1.68 eV on the interface. Spatially mapped X^-/X^0 integrated intensity ratio across the interface showing variations in the X^- intensity for (e) sample 1 and (f) sample 2. Spatially mapped H1/X^0 integrated intensity ratio across the interface showing changes in the H1 intensity in (g) sample 1 and (h) sample 2. The ratio X^-/X^0 correlates with changes in the H1/X^0 intensity at the interface.

spectra contain a previously unobserved feature, referred to as H1, at ≈1.68 eV. H1 is comparable to X^0 in both intensity and linewidth for sample 1, while being weaker and broader in sample 2.

The 5 K PL spectra also show the evidence of an anticorrelation between H1 and X^-. Spatially resolved PL maps of the interface allow us to explore this behavior further and connect it to interface quality by examining the integrated intensity ratios X^-/X^0 [Figs. 1(e) and 1(f)] and $H1/X^0$ [Figs. 1(g) and 1(h)]. H1 and $X^0 + X^-$ integrated intensities are plotted separately in Fig. S1 of the supplementary material. For sample 1, the ratio of X^-/X^0 [Fig. 1(e)] varies between 1 and 2 over most of the $MoSe_2$ flake with a notable jump at the crack on the bottom left quadrant of the map. On the heterostructure itself, this ratio plummets to well below 1, indicating the absence of free charges that can participate in trion formation. The connection of the X^-/X^0 ratio to charge transfer is well established in numerous reports[11–13,54] and, since the transfer efficiency is exponentially dependent on distance, can be used as a proxy for interlayer spacing. $MoSe_2$ tends to be n-type as-exfoliated, and $TiSe_2$ band alignment suggests that it will act as an electron acceptor.[55] Therefore, the near absence of X^- emission on the sample 1 overlap region suggests good

coupling between the $TiSe_2$–$MoSe_2$ flakes. For sample 2, the X^-/X^0 ratio [Fig. 1(f)] is larger on the $MoSe_2$ flake, varying between 3 and 6, which may originate from unintentional doping during the heterostructure fabrication process. On the $TiSe_2$–$MoSe_2$ overlap, we observe a reduction in the X^- intensity co-localized with H1 but smaller than in sample 1. From this, we suggest that interlayer coupling is weaker in sample 2, which could be due to contaminants or partial oxidation of the $TiSe_2$ flake. The remaining analyses will therefore focus on sample 1, unless otherwise noted.

B. Temperature and power dependence of H1

In this section, we discuss temperature- and power-dependent PL measurements on and off the $TiSe_2$–$MoSe_2$ interface. Figure 2(a) shows a temperature-dependent PL intensity map from 5 to 265 K taken on the interface in sample 1. A similar dataset for sample 2 is included in the supplementary material (Fig. S2). Here, the 5 K PL emission spectrum is the same as in Fig. 1(c) with prominent, sharp emission from X^0 and H1, heavily reduced X^- emission, and a broad feature originating from defects. With increasing temperature, PL from defect excitons and X^- decreases and becomes unobservable
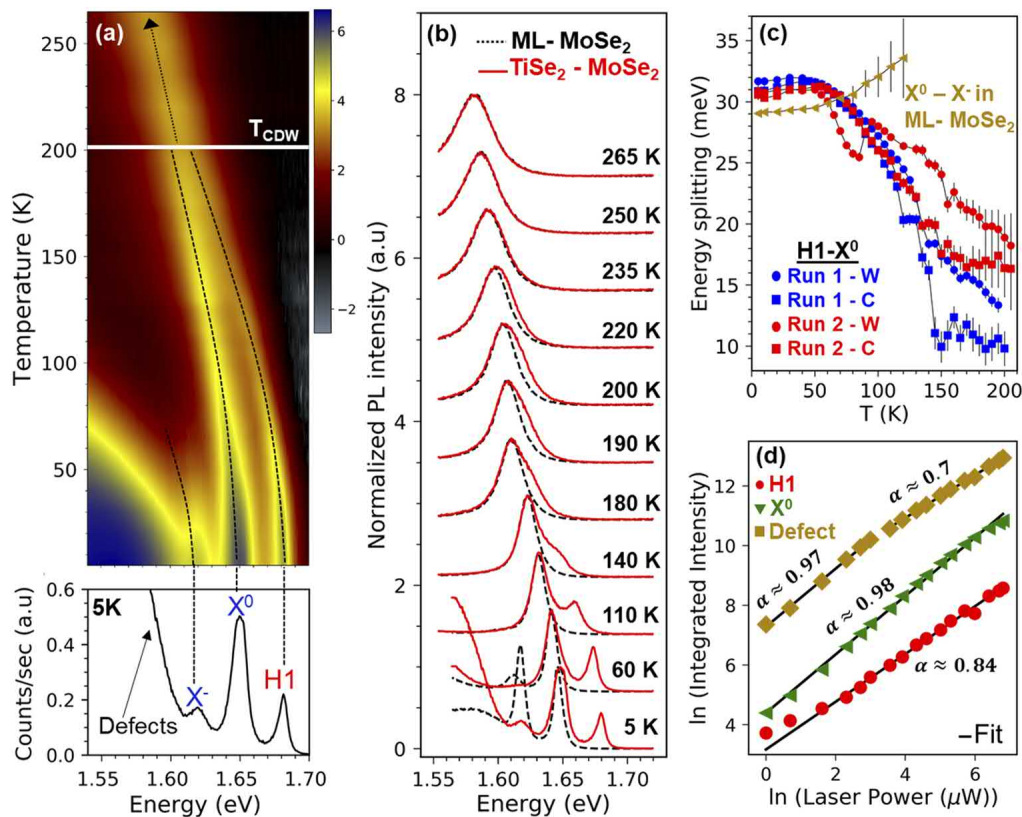
FIG. 2. (a) Temperature-dependent PL map on the $TiSe_2$–$MoSe_2$ interface of sample 1. The dashed lines are guides to the eye, and the 5 K PL spectrum beneath the map labels the optical transitions. T_{CDW} for bulk $TiSe_2$ is indicated by the horizontal white line. (b) Line shape analysis of PL spectra taken on (red) and off (black) the $TiSe_2$–$MoSe_2$ interface. The interface spectra have been shifted to align the X^0 emission energies between the two curves. (c) Energy separation between H1 and X^0 vs temperature for two separate runs (red, blue), each consisting of a warming (W, circles) and cooling (C, squares) curve. 1-σ error bars from fits to the PL spectra are included. X^0–X^- is included for ML–$MoSe_2$ to illustrate the difference from H1. (d) Log–log plot of the PL integrated intensity vs excitation laser power. The solid black lines are power-law fits to the data.

for $T > 70$ K in agreement with prior studies.[56–59] Both X^0 and H1 are visible at elevated temperatures but are difficult to distinguish above ≈190 K. We obtain a better understanding through the analysis of the PL line shape for ML–MoSe$_2$ and TiSe$_2$–MoSe$_2$. Figure 2(b) compares PL spectra at selected temperatures taken on (red curve) and off (black curve) the TiSe$_2$–MoSe$_2$ interface. The presence of the TiSe$_2$ capping layer causes X^0 to blueshift due to the different dielectric constant.[25,26] To facilitate comparison, we eliminate this shift by adjusting the energy axis of the TiSe$_2$–MoSe$_2$ spectrum so that the X^0 PL peaks overlap. The energy shift amounts to ~1–3 meV across the entire temperature range. H1 is visible as a weak shoulder of X^0 between 190 and 220 K. Above these temperatures, the PL line shape on and off the interface is identical, indicating that the driving mechanism behind H1 has dissipated. We also fit each PL spectrum to a sum of Lorentzian functions and extract the temperature-dependent peak parameters for H1, X^0, and X^-. The energy splitting, H1–X^0, is shown in Fig. 2(c) over two cooling and warming runs that extend up to 200 K. In both cases, the energy separation between H1 and X^0 decreases with temperature until 200 K after which it is difficult to obtain a reliable fit.

The temperature window of 190–220 K is apparently crucial to H1 and is known to be important for TiSe$_2$. Bulk 1T-TiSe$_2$ undergoes a $2 \times 2 \times 2$ commensurate-CDW transition in the range of $T_{CDW} \approx 200$–210 K, as observed in a variety of optical and electronic measurements.[39,60–62] The CDW transition opens a bandgap at the TiSe$_2$ M point in the Brillouin zone (BZ) with an associated order parameter well described by the Bardeen–Cooper–Schrieffer (BCS) model.[62] The observed correlation of H1 with T_{CDW} suggests a close relationship between H1 in MoSe$_2$ and the CDW in TiSe$_2$.

Power-dependent PL measurements provide further insight into the nature of H1, as presented for sample 1 in Fig. 2(d) and for sample 2 in the supplementary material (Fig. S2). The PL intensity generally scales with power as $I_{PL} \propto P^\alpha$, where I_{PL} is the integrated PL intensity and P is the excitation power. The exponent $\alpha \approx 1$ for free excitons and >1 for multiexcitons.[16] Localized exciton states exhibit a more complicated behavior. At low powers, $\alpha \sim 1$ but then becomes sublinear as the localized states are saturated.[59] These behaviors are observed in Fig. 2(d) where we plot the natural logarithms of I_{PL} and P. The linear fits to these data allow for the extraction of α. We find that both X^0 and H1 have an $\alpha \approx 1$, with the value for H1 being somewhat lower, suggesting free exciton characteristics. As expected, the defect band first exhibits $\alpha \approx 1$ at low powers and then shows signs of saturation with $\alpha \approx 0.7$. While α for H1 is lower than would be expected for a free exciton, the absence of saturation is more consistent with this interpretation.

C. CDW phase at the TiSe$_2$–MoSe$_2$ interface

Raman spectroscopy can probe the square of the CDW order parameter directly since the intensity of the symmetry-forbidden modes appears in the second order of the ionic displacements of the high-symmetry positions. Raman measurements performed at the TiSe$_2$–MoSe$_2$ interface in the range of 5–265 K are shown in Fig. 3(a). The 5 K Raman spectra show the CDW modes at E_g^{CDW} (70 cm^{-1}) and A_g^{CDW} (108 cm^{-1}), as well as normal TiSe$_2$ lattice modes at 132 and 200 cm^{-1} of E_g and A_{1g} symmetry, respectively.[63,64] The MoSe$_2$ A_{1g} mode is also visible at 245 cm^{-1} and is related to out-of-plane vibrations.[65] Figure 3(b) plots the
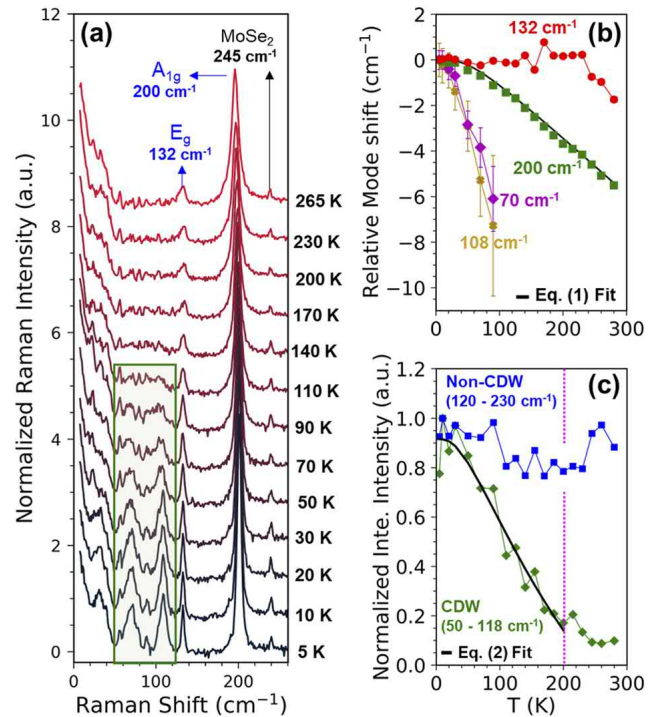

FIG. 3. (a) Temperature-dependent Raman spectra taken on the TiSe$_2$–MoSe$_2$ interface in sample 1. (b) Shift in the observed TiSe$_2$ Raman modes relative to the 5 K value. 1-σ error bars from spectral fitting are included. The solid black line is fit to Eq. (1) that accounts for optical phonon decay processes. (c) Normalized integrated Raman intensity of the CDW modes (green diamonds) and lattice modes (blue squares) vs temperature. The dotted magenta line indicates T_{CDW}. The solid black line is a fit to Eq. (2).

temperature-dependent shifts of all TiSe$_2$ modes relative to their frequency at 5 K. The 135 cm^{-1} mode is largely unaffected by temperature changes, blueshifting slightly as temperature is lowered and then stabilizing. The 200 cm^{-1} mode is insensitive to the CDW transition, and its anharmonicity can be understood by a combination of optical phonon decay and temperature-dependent changes in the lattice constants.[66] This is described by the following equation [solid black line in Fig. 3(b)]:

$$\Delta(\omega(0), T) = \omega_0 + A\left(1 + \frac{2}{e^x - 1}\right). \tag{1}$$

Here, $x = \hbar\omega_B/2k_B T$, ω_0 is the 0 K harmonic frequency, and A represents the anharmonic contributions to the frequency of the 200 cm^{-1} optical mode as it decays into two acoustic phonons. The obtained value for A = −1.85 cm^{-1} is within the ballpark of similar phonon anharmonicity studies done on TMDs.[67,68]

The CDW modes at 70 and 109 cm^{-1} redshift and broaden with increasing temperature. These modes are unresolved above $T = 100$ K, which is well below T_{CDW}. This behavior is commonly attributed to quantum fluctuations of the density wave.[69] Integrating the Raman intensity over the spectral range encompassing the CDW modes allows us to monitor the CDW up to the transition temperature [Fig. 3(c)]. Thermal melting of the CDW is expected to

follow a temperature dependence consistent with the BCS treatment where the order parameter $\Delta(T)$ can be given as[70]

$$\frac{\Delta^2(T)}{\Delta^2(0)} \propto \tanh^2\left(\alpha_{BCS}\sqrt{1-\frac{T}{T_{CDW}}}\right), \qquad (2)$$

where α_{BCS} is a constant determined by BCS theory but in practice can vary between materials. This model fits the integrated intensity data well up to T_{CDW}, as shown in Fig. 3(c).

III. DISCUSSION

Investigations into the properties of 2D excitons in TMDs have covered remarkable ground over the past decade.[9,10,71–73] Despite these remarkably comprehensive studies, no observations of vdW heterostructures have shown PL satellites above X^0. Therefore, we explore here three possible mechanisms that could be responsible for H1.

Before proceeding with the analysis of potential microscopic interpretations of the new peak, we summarize key experimental observations. First, H1 lies 25–32 meV above X^0 with an intensity that differs between samples (Fig. 1). Second, within a single sample, the relative intensity of H1 to X^0 is temperature independent [Fig. 4(a)]. Third, the energy difference between H1 and X^0 follows the CDW order parameter Δ^2. We illustrate this in Fig. 4(c) by overlaying neutron scattering data from Ref. 61, the energy separation H1–X^0, and the integrated intensity of the TiSe$_2$-CDW Raman features. Fourth, the intensity ratio H1/X^0 decreases with increasing laser power [Fig. 4(b)]. Finally, H1 and X^- are spatially anti-correlated (Fig. 1).

A. Mechanism I: Activation of forbidden/dark excitons

Semiconducting TMDs host numerous dark exciton states where optical recombination is forbidden by momentum conservation or symmetry. Density functional theory (DFT) calculations of MoSe$_2$ suggest that a finite-momentum dark exciton lies 30 meV above X^0.[74] This indirect exciton is formed from an electron residing at the $Q(Q')$ valley and a hole at the $K(K')$ valley [Fig. 4(e)]. The indirect exciton has not been observed experimentally in PL, but resonant Raman measurements offer some evidence for dark excitons above X^0.[75] While the energy of this exciton matches the energy of H1, a viable mechanism is required to provide the missing momentum needed for optical recombination of this dark state. Mechanism I explores how the interface between TiSe$_2$ and MoSe$_2$
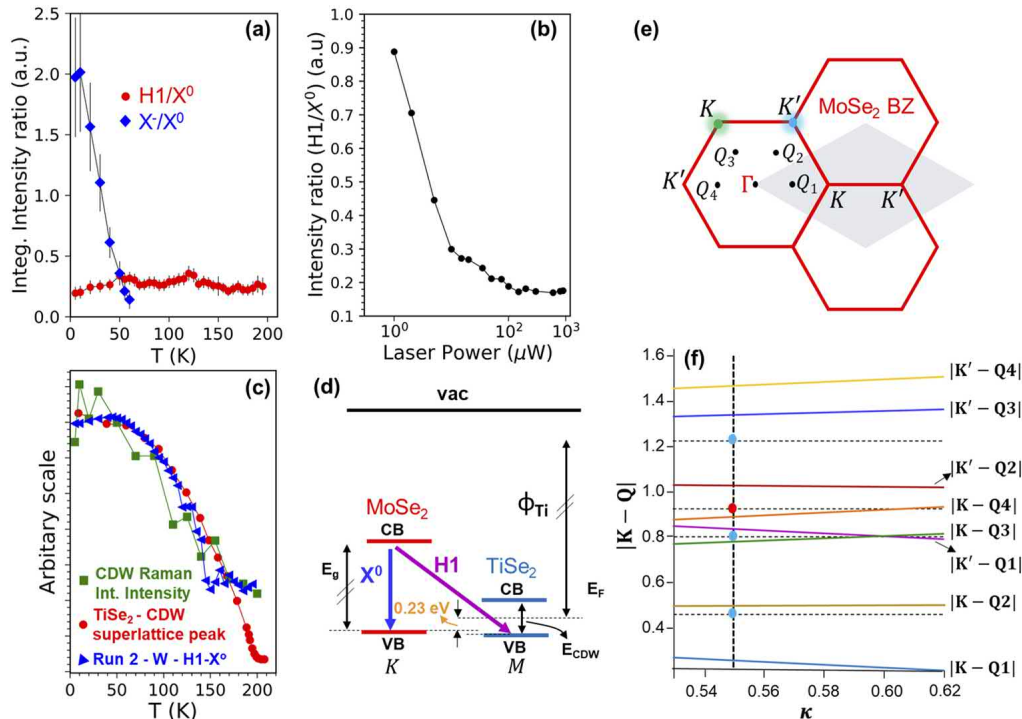

FIG. 4. (a) PL integrated intensity ratios H1/X^0 (red circles) and X^-/X^0 (blue diamonds) vs temperature. (b) H1/X^0 integrated intensity ratio vs the laser power (lin–log scale). (c) Overlay of the energy separation between H1 and X^0 for sample 1, the integrated Raman intensity of the CDW modes, and the TiSe$_2$ CDW superlattice peak extracted from neutron scattering data in Ref. 61, all versus temperature. (d) A schematic of a type-II band alignment at the TiSe$_2$–MoSe$_2$ interface leading to an interlayer exciton. (e) Brillouin zones for the MoSe$_2$ lattice and the corresponding reciprocal lattice unit cell (gray). (f) Lengths of the scattering vectors $|\mathbf{K}-\mathbf{Q}|$ in units of the MoSe$_2$ reciprocal lattice vectors (colored solid lines) compared to the length of the reciprocal lattice vectors of the undistorted (red dot) and CDW (blue dots) lattice in TiSe$_2$. The horizontal dashed lines are guides to the eye. The vertical dashed line is drawn to pass through $\kappa = 0.55$ to facilitate the comparison with the magnitude of the MoSe$_2$ wavevectors $|\mathbf{K}-\mathbf{Q}|$ and the smallest reciprocal lattice vector (dots) in TiSe$_2$.

could potentially activate such dark states by introducing a new spatial periodicity that violates quasimomentum conservation.

MoSe$_2$ and TiSe$_2$ form an incommensurate superstructure for most stacking configurations, which, formally, implies a full relaxation of quasimomentum conservation. In order to illustrate this, consider the MoSe$_2$ Bloch wave functions at the TiSe$_2$–MoSe$_2$ overlap. We assume that there is no hybridization between MoSe$_2$ and TiSe$_2$ wave functions, which is reasonable due to their large spatial separation. The quasimomentum can then be defined by the MoSe$_2$ lattice alone, and the Bloch functions are $\psi_{\mathbf{k}}(\mathbf{r})$ = $\sum_{\mathbf{g}} a_{\mathbf{k+g}} \exp[i(\mathbf{k} + \mathbf{g}) \cdot \mathbf{r}]$, where $\mathbf{g}$ is a MoSe$_2$ reciprocal lattice (r.l.) vector and $\mathbf{a}_{\mathbf{k+g}}$ are the Bloch coefficients. The presence of the TiSe$_2$ lattice and CDW can be thought of as a periodic "defect" for MoSe$_2$ that enables scattering between the K and Q points. The matrix element of the associated potential for Bloch states is $\langle \psi_{\mathbf{Q}}|V(\mathbf{r})|\psi_{\mathbf{K}} \rangle$, where $\mathbf{K}$ is a wavevector for any of the K-equivalent points and $\mathbf{Q}$ is a wavevector for any of the Q-equivalent ones [Fig. 4(e)]. $V(\mathbf{r})$ is the effective TiSe$_2$ defect potential, which can be expanded in the TiSe$_2$ r.l. vectors $\mathbf{t}$. Note that the lattice parameter for TiSe$_2$ is 7.8% larger than MoSe$_2$ so that if we measure the reciprocal space in units of $2\pi/a_{\text{MoSe}_2}$, then for Mo, the first r.l. vectors will be $\mathbf{g}_{1,2} = \{\sqrt{3}/2, \pm 1/2\}$; $\mathbf{g}_3 = \mathbf{g}_1 + \mathbf{g}_2$. For TiSe$_2$, the equivalent r.l. vectors $\mathbf{t}_{1,2,3}$ will be shorter by 7.8%.

Using the expansion of $V(\mathbf{r})$, we obtain

$$
\begin{aligned}
\langle \psi_{\mathbf{Q}}|V(\mathbf{r})|\psi_{\mathbf{K}} \rangle &= \sum_{\mathbf{t}} \left\langle \psi_{\mathbf{Q}} \middle| v_{\mathbf{t}} e^{i\mathbf{t}\cdot\mathbf{r}} \middle| \psi_{\mathbf{K}} \right\rangle \\
&= \sum_{\mathbf{t},\mathbf{g},\mathbf{g}'} \left\langle a_{\mathbf{K+g}} e^{i(\mathbf{K+g})\cdot\mathbf{r}} v_{\mathbf{t}} e^{i\mathbf{t}\cdot\mathbf{r}} a_{\mathbf{Q+g}'}^* e^{-i(\mathbf{Q+g}')\cdot\mathbf{r}} \right\rangle \\
&= \sum_{\mathbf{t},\mathbf{K},\mathbf{Q}} a_{\mathbf{K}} a_{\mathbf{Q}}^* v_{\mathbf{t}} \left\langle e^{i(\mathbf{K-Q+t})\cdot\mathbf{r}} \right\rangle \\
&= \sum_{\mathbf{t},\mathbf{K},\mathbf{Q}} a_{\mathbf{K}} a_{\mathbf{Q}}^* v_{\mathbf{t}} \delta(\mathbf{K} - \mathbf{Q} + \mathbf{t}).
\end{aligned}
$$

In the last line, the summation goes over all equivalent K and Q points. While, in principle, in an infinite lattice, one can always find a triad $\mathbf{K}, \mathbf{Q}, \mathbf{t}$ wavevectors that closely satisfies the condition $|\mathbf{K} - \mathbf{Q} + \mathbf{t}| = 0$, the coefficients $v_{\mathbf{t}}$ and, to lesser extent, $a_{\mathbf{g}}$ rapidly decay (the form factor effect), and so this scattering process can only be efficient if $|\mathbf{t}|$ is small.

Determining if the TiSe$_2$ "defect" potential can enable $K \to Q$ scattering requires matching $|\mathbf{t}|$ and $|\mathbf{K} - \mathbf{Q}|$. We have carried out DFT calculations of the TiSe$_2$–MoSe$_2$ heterostructure to determine how this position is altered by interlayer coupling. The location of the Q valley is $\kappa = |\mathbf{Q} - \mathbf{\Gamma}|/|\mathbf{K} - \mathbf{\Gamma}|$, which are clustered around 0.55 $\pm$ 0.05 for multiple DFT runs. The magnitude of the smallest scattering vectors $\mathbf{K} - \mathbf{Q}$ is $(1 - \kappa)/\sqrt{3}$, $(1 + \kappa)/\sqrt{3}$, $(\sqrt{1 - \kappa + \kappa^2})/\sqrt{3}$, $(\sqrt{1 + \kappa + \kappa^2})/\sqrt{3}$, $(2 - \kappa)/\sqrt{3}$, and $(\sqrt{4 - 2\kappa + \kappa^2})/\sqrt{3}$, where the first two values correspond to scattering from Q to K or K', while the next two values correspond to scattering from Q' to K or K', and the last two to scattering into the next BZ. For $\kappa = 0.55$, in units of $2\pi/a_{\text{MoSe}_2}$, these are 0.260, 0.895, 0.501, 0.785, 0.832, and 1.033, respectively. At the same time, the smallest vector of the r.l. of TiSe$_2$ without the CDW is $t_1 = 0.928(2\pi/a_{\text{Mo}})$.

In Fig. 4(e), we present the magnitude of the scattering wavevector $|\mathbf{K} - \mathbf{Q}|$ between different K and Q points vs κ in MoSe$_2$. These are compared to the r.l. vectors of TiSe$_2$ in the normal (blue

dots) and CDW (red dot) phases. The smallest TiSe$_2$ r.l. vector can only match one of the $|\mathbf{K} - \mathbf{Q}|$ values if κ is 0.607, which is far outside our DFT predictions. In the $2 \times 2 \times 2$ CDW phase of TiSe$_2$, the magnitude of the r.l. vectors (τ_i) are shortened to $\tau_1 = t_1/2$; $\tau_2 = t_1\sqrt{3}/2$; $\tau_3 = t_1$; $\tau_4 = \sqrt{7}/2t_1$. We find that particularly $\tau_2 = 0.804$ is close to the magnitude of one of the $\mathbf{K} - \mathbf{Q}$ vectors. This is shown by the red dot in Fig. 4(e). The mismatch is less than $0.019(2\pi/a_{\text{Mo}})$ and is reduced to zero for $\kappa = 0.59$, a value within the range of the DFT calculations.

Therefore, we conclude that the CDW potential opens a new $K \to Q$ scattering channel. This would enable optical recombination of an indirect, finite-momentum exciton, resulting in the appearance of a new PL line at the same energy as H1.[74] Future calculations taking into account the effect of the CDW–exciton coupling may be able to assess this scenario quantitatively, but such calculations are outside our current capabilities. This result explains the emission energy of H1, its disappearance at T_{CDW}, and its anticorrelation with X$^-$. However, this mechanism would also imply H1–X^0 (barring unrelated phenomena) to be T-independent and the H1/X^0 intensity ratio to follow Δ^2. Our observations indicate just the opposite [Figs. 4(a) and 4(c)]. Furthermore, this mechanism cannot explain the decrease in the H1/X^0 intensity ratio with excitation power in Fig. 4(b).

B. Mechanism II: Interlayer 2D TiSe$_2$–MoSe$_2$ exciton

Another intriguing possibility is the formation of an interlayer exciton by an electron in MoSe$_2$ and a hole in the TiSe$_2$ layer, as shown in Fig. 4(d). This is only possible due to the opening of the CDW bandgap in the low-temperature regime but is inconceivable in the normal metallic phase. The intensity of such an exciton will be defined by (T-independent) interlayer tunneling, and the position will be, roughly, given by $E_c(\text{MoSe}_2) - E_F(\text{TiSe}_2) - E_{CDW}(\text{TiSe}_2)/2$. The energy gap, E_{CDW}, is proportional to the order parameter Δ^2, and its value is unclear: Experiments cite different numbers, and most angle-resolved photoemission spectroscopy studies find the top of the valence band to be separated from the Fermi level (i.e., half the bandgap) by 50–75 meV,[62,76] qualitatively consistent with the H1–X^0 separation, and roughly following Δ^2.

For this scenario to be realized, the top of the Mo valence band at K should fall inside the CDW gap in TiSe$_2$ (or, equivalently, within a few tens of meV from the TiSe$_2$ Fermi energy, E_F, in the metallic phase). Our standard DFT calculations using a supercell with 2×2 periodicity in TiSe$_2$ and $\sqrt{7} \times \sqrt{39}$ in MoSe$_2$ (Ti$_{16}$Mo$_{19}$) show that E_F is about 230 meV above the MoSe$_2$ valence band. This is illustrated in Fig. 4(d) and detailed in Sec. S3 of the supplementary material. Hence, while this naturally explains all five experimental observations it also requires an assumption that the DFT calculations of the band alignment are off by 100–150 meV, which may be reasonable once the electronic correlations that drive the CDW formation and the details of the vdW interface are properly included.

C. Mechanism III: Exciton–phonon and exciton–plasmon interaction

Exciton formation and recombination can, in principle, be assisted through coupling to a variety of bosonic excitations. Again focusing on the activation of a dark finite-momentum exciton, the

lowest energy phonon with the appropriate momentum has an energy of ~10 meV[77] so that the corresponding PL energy should be shifted down (phonon-assisted emission) from the momentum dark exciton energy. This would suggest that H1 is a phonon replica of a higher-energy exciton, either symmetry forbidden or momentu-indirect. However, this mechanism is unlikely considering that it is intrinsic to MoSe$_2$ and cannot explain the role of the TiSe$_2$ CDW. In principle, interlayer coupling could allow TiSe$_2$ phonons to create exciton–phonon replicas in MoSe$_2$. H1 should in this case emerge at higher temperature if TiSe$_2$ phonons are involved, and the replica would show additional temperature dependence compared to X^0, in contradiction with our observation.[78–80] An additional possibility regarding the activation of a finite-momentum exciton by coupling to TiSe$_2$ is the presence of a distinct low-energy plasmon. A curious aspect of the TiSe$_2$-CDW transition is the presence of a low-energy plasmon, which has been claimed as evidence of the excitonic insulator mechanism,[81] although this claim was later disputed.[82] This plasmon was measured to have an energy of $\hbar\omega_{pl}(q) \approx 50$ meV at $T = 17$ K with $q = 0$. This excitation was found to soften with temperature, reaching $\hbar\omega_{pl} \approx 35$ meV at $T = 185$ K. The plasmon is only present in the CDW phase, so it is tempting to associate it with the H1 PL line.

Signatures of exciton–plasmon interaction in PL have attracted considerable attention recently.[83–86] While these papers consider excitons and plasmons spatially coexisting in the same material, the theory is equally applicable to spatially separated MoSe$_2$ excitons and TiSe$_2$ plasmons, as long as they are coupled by the Coulomb interaction. In principle, two mechanisms are possible (see Sec. S4 of the supplementary material for a detailed discussion): The exciton Green function can be renormalized by a virtual process of emission and absorption of a plasmon or a process with either emission or absorption of a real plasmon. The former process shifts the exciton line E_X up by a fixed amount, which in the first approximation can be expressed as $E_X^2 - E_{X0}^2 \approx 4|\mathcal{M}|^2 E_{X0}\hbar\omega_{pl}/(E_{X0}^2 - (\hbar\omega_{pl})^2) \approx 4|\mathcal{M}|^2 \hbar\omega_{pl}/E_{X0}$, where E_{X0} is the position of X^0 in the absence of exciton–plasmon coupling and $\mathcal{M}$ is the exciton–plasmon coupling constant. However, one would expect the coupling constant to vary spatially, so instead of two lines one would observe a broad manifold starting at E_{X0} and ending at around $E_{X0} + 2|\mathcal{M}|^2\hbar\omega_{pl}/E_{X0}$, in contradiction with the experiment. The other mechanism preserves the main line and adds two satellites, shifted down and up by around ω_{pl}. The intensity of the upper peak is roughly temperature independent, and the intensity of the lower peak is proportional to the population of thermally or extrinsically excited plasmons. We do not observe the lower satellite at all, and the upper satellite, H1, only loses its intensity with temperature [Fig. 2(b)] and with the laser power [Fig. 4(b)], in obvious contradiction with the assumed physics.

D. Summary of possible mechanisms

We have presented here three speculative scenarios by which a new feature may appear in the PL of a TiSe$_2$–MoSe$_2$ heterostructure. While none can fully capture the entire scope of our observations, we conclude that the dark exciton and interlayer exciton interpretations are the most likely explanations for H1. While the plasmon model is exciting due to its connection to TiSe$_2$ excitonic-insulator physics, it appears less likely to be important for this particular heterostructure.

IV. CONCLUSION

We have discovered the presence of a new exciton-like peak in TiSe$_2$–MoSe$_2$ heterostructures using temperature-dependent PL spectroscopy. The H1 emission feature is localized to the heterostructure interface and correlated with T_{CDW} in TiSe$_2$. We have presented multiple scenarios that could explain the origin of this feature. The most plausible explanations of H1 are, presently, (1) an interlayer TiSe$_2$–MoSe$_2$ exciton and (2) the brightening of momentum dark excitons by the CDW potential. These results are the first demonstration of exciton engineering via proximitized CDWs and provide the 2D theoretical community with a fresh challenge to understand the microscopic mechanisms underlying CDW–exciton interactions.

V. GROWTH OF TMD MATERIALS

MoSe$_2$ crystals were grown by the chemical vapor transport (CVT) method using polycrystalline MoSe$_2$ powder (≈ 1 g) and SeBr$_4$ transport agent (≈ 0.1 g). The source and growth zones in a vacuum-sealed 20 cm long quartz ampoule were kept at 980 and 890 °C, respectively, for seven days. The procedure for CVT-grown TiSe$_2$ crystals is outlined in Ref. 39.

VI. SAMPLE PREPARATION, ASSEMBLY, AND AFM "NANO-SQUEEGEE"

Bulk-hBN flakes were mechanically exfoliated and transferred on O$_2$ plasma cleaned Si/SiO$_2$ substrates. MLs of 2H–MoSe$_2$ obtained through mechanical exfoliation were subsequently transferred on an identified hBN flake. For both materials, the transfer process was done using the PDMS-based dry viscoelastic stamping method.[49] This method has been known to leave polymer residues between the interface of two TMDs deposited during the transfer process but has proven to be optimal for fabricating heterostructures.[7] To create clean interfaces, an AFM-based "nano-squeegee" procedure was employed.[50] This involves the use of a standard AFM tip to push out polymer residues deposited between the two TMDs in a vertical heterostructure. We were able to use the same method to also remove surface residues present on the ML–MoSe$_2$ flake, using a 7 N/m spring constant tip and a contact force of 140 nN. Bulk TiSe$_2$ is then brought into contact with the sample using the same dry-transfer technique as done for ML–MoSe$_2$. The sample was additionally vacuum annealed at 200 °C for 5 h to improve coupling.

VII. EXPERIMENTAL SETUP

Low-temperature PL and Raman measurements were carried out on a confocal microscope setup with 532 nm laser excitation focused through a 0.42 NA, 50× long working-distance objective to achieve a spot diameter of 2.4 μm. The light is collected in a back-scattering geometry, with the collection fiber-coupled to a 500 mm focal length single spectrometer integrated with a liquid-N$_2$ cooled charge-coupled device detector. The samples were placed under vacuum and cooled in a closed cycle He-cooled cryostat (Montana Instruments Corporation) with a variable temperature range from 4 to 300 K. Raman measurements on the TiSe$_2$–MoSe$_2$ interface were carried out using the same setup; however, the excitation path included a collection of Bragg grating

notch filters enabling the acquisition of data within 15 cm^{-1} of the laser line. The excitation wavelength used for Raman measurements was 532 nm, and the laser power was kept at 300 μW pre-objective. Spatially resolved and temperature-dependent PL measurements were done using the same laser wavelength, while the power was kept within 150 μW pre-objective.

SUPPLEMENTARY MATERIAL

Additional spatially resolved PL measurements of samples 1 and 2, temperature and power-dependent measurements of sample 2, DFT calculations of the TiSe$_2$–MoSe$_2$ heterostructure, and a theoretical model of exciton–plasmon coupling are included in the supplementary material.

AUTHOR DECLARATIONS

Conflict of Interest

The authors have no conflicts to disclose.

DATA AVAILABILITY

The data that support the findings of this study are available from the corresponding author upon reasonable request.

REFERENCES

[1]I. Žutić, A. Matos-Abiague, B. Scharf, H. Dery, and K. Belashchenko, "Proximitized materials," Mater. Today **22**, 85–107 (2019).
[2]A. K. Geim and I. V. Grigorieva, "Van der Waals heterostructures," Nature **499**, 419–425 (2013).
[3]R. Bistritzer and A. H. MacDonald, "Moiré bands in twisted double-layer graphene," Proc. Natl. Acad. Sci. U. S. A. **108**, 12233–12237 (2011).
[4]Y. Cao, V. Fatemi, S. Fang, K. Watanabe, T. Taniguchi, E. Kaxiras, and P. Jarillo-Herrero, "Unconventional superconductivity in magic-angle graphene superlattices," Nature **556**, 43–50 (2018).

[5]K. Tran, G. Moody, F. Wu, X. Lu, J. Choi, K. Kim, A. Rai, D. A. Sanchez, J. Quan, A. Singh, J. Embley, A. Zepeda, M. Campbell, T. Autry, T. Taniguchi, K. Watanabe, N. Lu, S. K. Banerjee, K. L. Silverman, S. Kim, E. Tutuc, L. Yang, A. H. MacDonald, and X. Li, "Evidence for moiré excitons in van der Waals heterostructures," Nature **567**, 71–75 (2019).
[6]H. Yu, G. B. Liu, J. Tang, X. Xu, and W. Yao, "Moiré excitons: From programmable quantum emitter arrays to spin-orbit-coupled artificial lattices," Sci. Adv. **3**, e1701696 (2017).
[7]R. Frisenda, E. Navarro-Moratalla, P. Gant, D. Pérez De Lara, P. Jarillo-Herrero, R. V. Gorbachev, and A. Castellanos-Gomez, "Recent progress in the assembly of nanodevices and van der Waals heterostructures by deterministic placement of 2D materials," Chem. Soc. Rev. **47**, 53–68 (2018).
[8]M. Onodera, S. Masubuchi, R. Moriya, and T. Machida, "Assembly of van der Waals heterostructures: Exfoliation, searching, and stacking of 2D materials," Jpn. J. Appl. Phys., Part 1 **59**, 010101 (2020).
[9]G. Wang, A. Chernikov, M. M. Glazov, T. F. Heinz, X. Marie, T. Amand, and B. Urbaszek, "Colloquium: Excitons in atomically thin transition metal dichalcogenides," Rev. Mod. Phys. **90**, 021001 (2018).
[10]T. Mueller and E. Malic, "Exciton physics and device application of two-dimensional transition metal dichalcogenide semiconductors," npj 2D Mater. Appl. **2**, 29 (2018).
[11]J. S. Ross, S. Wu, H. Yu, N. J. Ghimire, A. M. Jones, G. Aivazian, J. Yan, D. G. Mandrus, D. Xiao, W. Yao, and X. Xu, "Electrical control of neutral and charged excitons in a monolayer semiconductor," Nat. Commun. **4**, 1474 (2013).
[12]Z. Li, T. Wang, S. Miao, Z. Lian, and S.-F. Shi, "Fine structures of valley-polarized excitonic states in monolayer transitional metal dichalcogenides," Nanophotonics **9**, 1811–1829 (2020).
[13]Z. Li, T. Wang, Z. Lu, C. Jin, Y. Chen, Y. Meng, Z. Lian, T. Taniguchi, K. Watanabe, S. Zhang, D. Smirnov, and S.-F. Shi, "Revealing the biexciton and trion-exciton complexes in BN encapsulated WSe$_2$," Nat. Commun. **9**, 3719 (2018).
[14]Z. Ye, L. Waldecker, E. Y. Ma, D. Rhodes, A. Antony, B. Kim, X.-X. Zhang, M. Deng, Y. Jiang, Z. Lu, D. Smirnov, K. Watanabe, T. Taniguchi, J. Hone, and T. F. Heinz, "Efficient generation of neutral and charged biexcitons in encapsulated WSe$_2$ monolayers," Nat. Commun. **9**, 3718 (2018).
[15]S.-Y. Chen, T. Goldstein, T. Taniguchi, K. Watanabe, and J. Yan, "Coulomb-bound four- and five-particle intervalley states in an atomically-thin semiconductor," Nat. Commun. **9**, 3717 (2018).
[16]M. Barbone, A. R.-P. Montblanch, D. M. Kara, C. Palacios-Berraquero, A. R. Cadore, D. De Fazio, B. Pingault, E. Mostaani, H. Li, B. Chen, K. Watanabe, T. Taniguchi, S. Tongay, G. Wang, A. C. Ferrari, and M. Atatüre, "Charge-tuneable biexciton complexes in monolayer WSe$_2$," Nat. Commun. **9**, 3721 (2018).
[17]C. Robert, B. Han, P. Kapuscinski, A. Delhomme, C. Faugeras, T. Amand, M. R. Molas, M. Bartos, K. Watanabe, T. Taniguchi, B. Urbaszek, M. Potemski, and X. Marie, "Measurement of the spin-forbidden dark excitons in MoS$_2$ and MoSe$_2$ monolayers," Nat. Commun. **11**, 4037 (2020).
[18]Z. Lu, D. Rhodes, Z. Li, D. V. Tuan, Y. Jiang, J. Ludwig, Z. Jiang, Z. Lian, S.-F. Shi, J. Hone, H. Dery, and D. Smirnov, "Magnetic field mixing and splitting of bright and dark excitons in monolayer MoSe$_2$," 2D Mater. **7**, 15017 (2019).
[19]E. Malic, M. Selig, M. Feierabend, S. Brem, D. Christiansen, F. Wendler, A. Knorr, and G. Berghäuser, "Dark excitons in transition metal dichalcogenides," Phys. Rev. Mater. **2**, 014002 (2018).
[20]X.-X. Zhang, T. Cao, Z. Lu, Y.-C. Lin, F. Zhang, Y. Wang, Z. Li, J. C. Hone, J. A. Robinson, D. Smirnov, S. G. Louie, and T. F. Heinz, "Magnetic brightening and control of dark excitons in monolayer WSe$_2$," Nat. Nanotechnol. **12**, 883–888 (2017).
[21]W.-t. Hsu, J. Quan, C.-y. Wang, L.-s. Lu, M. Campbell, W.-h. Chang, L.-J. Li, X. Li, and C.-K. Shih, "Dielectric impact on exciton binding energy and quasiparticle bandgap in monolayer WS$_2$ and WSe$_2$," 2D Mater. **6**, 025028 (2019).
[22]M. Florian, M. Hartmann, A. Steinhoff, J. Klein, A. W. Holleitner, J. J. Finley, T. O. Wehling, M. Kaniber, and C. Gies, "The dielectric impact of layer distances on exciton and trion binding energies in van der Waals heterostructures," Nano Lett. **18**, 2725–2732 (2018).
[23]S. Borghardt, J.-S. Tu, F. Winkler, J. Schubert, W. Zander, K. Leosson, and B. E. Kardynał, "Engineering of optical and electronic bandgaps in transition

metal dichalcogenide monolayers through external dielectric screening," Phys. Rev. Mater. **1**, 054001 (2017).

[24] A. V. Stier, N. P. Wilson, G. Clark, X. Xu, and S. A. Crooker, "Probing the influence of dielectric environment on excitons in monolayer WSe$_2$: Insight from high magnetic fields," Nano Lett. **16**, 7054–7060 (2016).

[25] A. Raja, A. Chaves, J. Yu, G. Arefe, H. M. Hill, A. F. Rigosi, T. C. Berkelbach, P. Nagler, C. Schüller, T. Korn, C. Nuckolls, J. Hone, L. E. Brus, T. F. Heinz, D. R. Reichman, and A. Chernikov, "Coulomb engineering of the bandgap and excitons in two-dimensional materials," Nat. Commun. **8**, 15251 (2017).

[26] A. Raja, L. Waldecker, J. Zipfel, Y. Cho, S. Brem, J. D. Ziegler, M. Kulig, T. Taniguchi, K. Watanabe, E. Malic, T. F. Heinz, T. C. Berkelbach, and A. Chernikov, "Dielectric disorder in two-dimensional materials," Nat. Nanotechnol. **14**, 832–837 (2019).

[27] Y. Jiang, S. Chen, W. Zheng, B. Zheng, and A. Pan, "Interlayer exciton formation, relaxation, and transport in TMD van der Waals heterostructures," Light: Sci. Appl. **10**, 72 (2021).

[28] A. T. Hanbicki, H.-J. Chuang, M. R. Rosenberger, C. S. Hellberg, S. V. Sivaram, K. M. McCreary, I. I. Mazin, and B. T. Jonker, "Double indirect interlayer exciton in a MoSe$_2$/WSe$_2$ van der Waals heterostructure," ACS Nano **12**, 4719–4726 (2018).

[29] B. Miller, A. Steinhoff, B. Pano, J. Klein, F. Jahnke, A. Holleitner, and U. Wurstbauer, "Long-lived direct and indirect interlayer excitons in van der Waals heterostructures," Nano Lett. **17**, 5229–5237 (2017).

[30] N. Zhang, A. Surrente, M. Baranowski, D. K. Maude, P. Gant, A. Castellanos-Gomez, and P. Plochocka, "Moiré intralayer excitons in a MoSe$_2$/MoS$_2$ heterostructure," Nano Lett. **18**, 7651–7657 (2018).

[31] T. Norden, C. Zhao, P. Zhang, R. Sabirianov, A. Petrou, and H. Zeng, "Giant valley splitting in monolayer WS$_2$ by magnetic proximity effect," Nat. Commun. **10**, 4163 (2019).

[32] L. Ciorciaro, M. Kroner, K. Watanabe, T. Taniguchi, and A. Imamoglu, "Observation of magnetic proximity effect using resonant optical spectroscopy of an electrically tunable MoSe$_2$/CrBr$_3$ heterostructure," Phys. Rev. Lett. **124**, 197401 (2020).

[33] B. Scharf, G. Xu, A. Matos-Abiague, and I. Žutić, "Magnetic proximity effects in transition-metal dichalcogenides: Converting excitons," Phys. Rev. Lett. **119**, 127403 (2017).

[34] D. Zhong, K. L. Seyler, X. Linpeng, R. Cheng, N. Sivadas, B. Huang, E. Schmidgall, T. Taniguchi, K. Watanabe, M. A. McGuire, W. Yao, D. Xiao, K. C. Fu, and X. Xu, "Van der Waals engineering of ferromagnetic semiconductor heterostructures for spin and valleytronics," Sci. Adv. **3**, e1603113 (2017).

[35] G. Xu, T. Zhou, B. Scharf, and I. Žutić, "Optically probing tunable band topology in atomic monolayers," Phys. Rev. Lett. **125**, 157402 (2020).

[36] Y. Zhou, J. Sung, E. Brutschea, I. Esterlis, Y. Wang, G. Scuri, R. J. Gelly, H. Heo, T. Taniguchi, K. Watanabe, G. Zaránd, M. D. Lukin, P. Kim, E. Demler, and H. Park, "Bilayer Wigner crystals in a transition metal dichalcogenide heterostructure," Nature **595**, 48–52 (2021).

[37] E. Liu, T. Taniguchi, K. Watanabe, N. M. Gabor, Y.-T. Cui, and C. H. Lui, "Excitonic and valleytronic signatures of correlated states at fractional fillings of a moiré superlattice," Phys. Rev. Lett. **127**, 037402 (2020).

[38] S. Miao, T. Wang, X. Huang, D. Chen, Z. Lian, C. Wang, M. Blei, T. Taniguchi, K. Watanabe, S. Tongay, Z. Wang, D. Xiao, Y.-T. Cui, and S.-F. Shi, "Strong interaction between interlayer excitons and correlated electrons in WSe$_2$/WS$_2$ moiré superlattice," Nat. Commun. **12**, 3608 (2021).

[39] A. A. Balandin, S. V. Zaitsev-Zotov, and G. Grüner, "Charge-density-wave quantum materials and devices–New developments and future prospects," Appl. Phys. Lett. **119**, 170401 (2021).

[40] K. Rossnagel, L. Kipp, and M. Skibowski, "Charge-density-wave phase transition in 1T–TiSe$_2$: Excitonic insulator versus band-type Jahn–Teller mechanism," Phys. Rev. B **65**, 235101 (2002).

[41] T. Pillo, J. Hayoz, H. Berger, and F. Lévy, "Photoemission of bands above the Fermi level: The excitonic insulator phase transition," Phys. Rev. B **61**, 16213–16222 (2000).

[42] H. Cercellier, C. Monney, F. Clerc, C. Battaglia, L. Despont, M. G. Garnier, H. Beck, P. Aebi, L. Patthey, H. Berger, and L. Forró, "Evidence for an excitonic insulator phase in 1T–TiSe$_2$," Phys. Rev. Lett. **99**, 146403 (2007).

[43] D. J. Campbell, C. Eckberg, P. Y. Zavalij, H.-H. Kung, E. Razzoli, M. Michiardi, C. Jozwiak, A. Bostwick, E. Rotenberg, A. Damascelli, and J. Paglione, "Intrinsic insulating ground state in transition metal dichalcogenide TiSe$_2$," Phys. Rev. Mater. **3**, 053402 (2019).

[44] M. He, P. Rivera, D. Van Tuan, N. P. Wilson, M. Yang, T. Taniguchi, K. Watanabe, J. Yan, D. G. Mandrus, H. Yu, H. Dery, W. Yao, and X. Xu, "Valley phonons and exciton complexes in a monolayer semiconductor," Nat. Commun. **11**, 618 (2020).

[45] E. Liu, J. van Baren, C.-T. Liang, T. Taniguchi, K. Watanabe, N. M. Gabor, Y.-C. Chang, and C. H. Lui, "Multipath optical recombination of intervalley dark excitons and trions in monolayer WSe$_2$," Phys. Rev. Lett. **124**, 196802 (2020).

[46] S. Brem, A. Ekman, D. Christiansen, F. Katsch, M. Selig, C. Robert, X. Marie, B. Urbaszek, A. Knorr, and E. Malic, "Phonon-assisted photoluminescence from indirect excitons in monolayers of transition-metal dichalcogenides," Nano Lett. **20**, 2849–2856 (2020).

[47] Z. Li, T. Wang, C. Jin, Z. Lu, Z. Lian, Y. Meng, M. Blei, S. Gao, T. Taniguchi, K. Watanabe, T. Ren, S. Tongay, L. Yang, D. Smirnov, T. Cao, and S.-F. Shi, "Emerging photoluminescence from the dark-exciton phonon replica in monolayer WSe$_2$," Nat. Commun. **10**, 2469 (2019).

[48] Z. Li, T. Wang, S. Miao, Y. Li, Z. Lu, C. Jin, Z. Lian, Y. Meng, M. Blei, T. Taniguchi, K. Watanabe, S. Tongay, W. Yao, D. Smirnov, C. Zhang, and S.-F. Shi, "Phonon-exciton Interactions in WSe$_2$ under a quantizing magnetic field," Nat. Commun. **11**, 3104 (2020).

[49] A. Castellanos-Gomez, M. Buscema, R. Molenaar, V. Singh, L. Janssen, H. S. J. van der Zant, and G. A. Steele, "Deterministic transfer of two-dimensional materials by all-dry viscoelastic stamping," 2D Mater. **1**, 011002 (2014).

[50] M. R. Rosenberger, H.-J. Chuang, K. M. McCreary, A. T. Hanbicki, S. V. Sivaram, and B. T. Jonker, "Nano-'Squeegee' for the creation of clean 2D material interfaces," ACS Appl. Mater. Interfaces **10**, 10379–10387 (2018).

[51] O. A. Ajayi, J. V. Ardelean, G. D. Shepard, J. Wang, A. Antony, T. Taniguchi, K. Watanabe, T. F. Heinz, S. Strauf, X.-Y. Zhu, and J. C. Hone, "Approaching the intrinsic photoluminescence linewidth in transition metal dichalcogenide monolayers," 2D Mater. **4**, 031011 (2017).

[52] J. Wierzbowski, J. Klein, F. Sigger, C. Straubinger, M. Kremser, T. Taniguchi, K. Watanabe, U. Wurstbauer, A. W. Holleitner, M. Kaniber, K. Müller, and J. J. Finley, "Direct exciton emission from atomically thin transition metal dichalcogenide heterostructures near the lifetime limit," Sci. Rep. **7**, 12383 (2017).

[53] J. Jadczak, J. Kutrowska-Girzycka, P. Kapuściński, Y. S. Huang, A. Wójs, and L. Bryja, "Probing of free and localized excitons and trions in atomically thin WSe$_2$, WS$_2$, MoSe$_2$ and MoS$_2$ in photoluminescence and reflectivity experiments," Nanotechnology **28**, 395702 (2017).

[54] E. Liu, J. van Baren, Z. Lu, M. M. Altaiary, T. Taniguchi, K. Watanabe, D. Smirnov, and C. H. Lui, "Gate tunable dark trions in monolayer WSe$_2$," Phys. Rev. Lett. **123**, 027401 (2019).

[55] C. Zhang, C. Gong, Y. Nie, K.-A. Min, C. Liang, Y. J. Oh, H. Zhang, W. Wang, S. Hong, L. Colombo, R. M. Wallace, and K. Cho, "Systematic study of electronic structure and band alignment of monolayer transition metal dichalcogenides in van der Waals heterostructures," 2D Mater. **4**, 015026 (2016).

[56] R. Sharma, J. Pandey, K. R. Sahoo, K. S. Rana, R. K. Biroju, W. Theis, A. Soni, and T. N. Narayanan, "Spectroscopic correlation of chalcogen defects in atomically thin MoS$_{2(1-x)}$Se$_{2x}$ alloys," J. Phys. Mater. **3**, 045001 (2020).

[57] T. Verhagen, V. L. P. Guerra, G. Haider, M. Kalbac, and J. Vejpravova, "Towards the evaluation of defects in MoS$_2$ using cryogenic photoluminescence spectroscopy," Nanoscale **12**, 3019–3028 (2020).

[58] M. Tangi, M. K. Shakfa, P. Mishra, M.-Y. Li, M.-H. Chiu, T. K. Ng, L.-J. Li, and B. S. Ooi, "Anomalous photoluminescence thermal quenching of sandwiched single layer MoS$_2$," Opt. Mater. Express **7**, 3697 (2017).

[59] S. Tongay, J. Suh, C. Ataca, W. Fan, A. Luce, J. S. Kang, J. Liu, C. Ko, R. Raghunathanan, J. Zhou, F. Ogletree, J. Li, J. C. Grossman, and J. Wu, "Defects activated photoluminescence in two-dimensional semiconductors: Interplay between bound, charged and free excitons," Sci. Rep. **3**, 2657 (2013).

[60] K. Sugawara, Y. Nakata, R. Shimizu, P. Han, T. Hitosugi, T. Sato, and T. Takahashi, "Unconventional charge-density-wave transition in monolayer 1T–TiSe$_2$," ACS Nano **10**, 1341–1345 (2016).

[61] F. J. Di Salvo, D. E. Moncton, and J. V. Waszczak, "Electronic properties and superlattice formation in the semimetal TiSe$_2$," Phys. Rev. B **14**, 4321–4328 (1976).

[62] P. Chen, Y.-H. Chan, X.-Y. Fang, S.-K. Mo, Z. Hussain, A.-V. Fedorov, M. Y. Chou, and T.-C. Chiang, "Hidden order and dimensional crossover of the charge density waves in TiSe₂," Sci. Rep. **6**, 37910 (2016).

[63] D. L. Duong, G. Ryu, A. Hoyer, C. Lin, M. Burghard, and K. Kern, "Raman characterization of the charge density wave phase of 1T–TiSe₂: From bulk to atomically thin layers," ACS Nano **11**, 1034–1040 (2017).

[64] C. S. Snow, J. F. Karpus, S. L. Cooper, T. E. Kidd, and T.-C. Chiang, "Quantum melting of the charge density wave state in 1T–TiSe₂," Phys. Rev. Lett. **91**, 136402 (2003).

[65] P. Tonndorf, R. Schmidt, P. Böttger, X. Zhang, J. Börner, A. Liebig, M. Albrecht, C. Kloc, O. Gordan, D. R. T. Zahn, S. Michaelis de Vasconcellos, and R. Bratschitsch, "Photoluminescence emission and Raman response of monolayer MoS₂, MoSe₂, and WSe₂," Opt. Express **21**, 4908 (2013).

[66] M. Balkanski, R. F. Wallis, and E. Haro, "Anharmonic effects in light scattering due to optical phonons in silicon," Phys. Rev. B **28**, 1928–1934 (1983).

[67] J. Joshi, I. R. Stone, R. Beams, S. Krylyuk, I. Kalish, A. V. Davydov, and P. M. Vora, "Phonon anharmonicity in bulk T_d-MoTe₂," Appl. Phys. Lett. **109**, 031903 (2016).

[68] L. Su, Y. Zhang, Y. Yu, and L. Cao, "Dependence of coupling of quasi 2-D MoS₂ with substrates on substrate types, probed by temperature dependent Raman scattering," Nanoscale **6**, 4920–4927 (2014).

[69] G. Grüner, *Density Waves in Solids* (CRC Press, 1994).

[70] P. Wölfle, "Theory of sound propagation in pair-correlated Fermi liquids: Application to ³He-B," Phys. Rev. B **14**, 89–113 (1976).

[71] K. F. Mak, C. Lee, J. Hone, J. Shan, and T. F. Heinz, "Atomically thin MoS₂: A new direct-gap semiconductor," Phys. Rev. Lett. **105**, 136805 (2010).

[72] S. Shree, I. Paradisanos, X. Marie, C. Robert, and B. Urbaszek, "Guide to optical spectroscopy of layered semiconductors," Nat. Rev. Phys. **3**, 39–54 (2021).

[73] D. Unuchek, A. Ciarrocchi, A. Avsar, K. Watanabe, T. Taniguchi, and A. Kis, "Room-temperature electrical control of exciton flux," Nature **560**, 340–344 (2018).

[74] T. Deilmann and K. S. Thygesen, "Finite-momentum exciton landscape in mono- and bilayer transition metal dichalcogenides," 2D Mater. **6**, 035003 (2019).

[75] L. P. McDonnell, J. J. S. Viner, P. Rivera, X. Xu, and D. C. Smith, "Observation of intravalley phonon scattering of 2s excitons in MoSe₂ and WSe₂ monolayers," 2D Mater. **7**, 045008 (2020).

[76] C. Monney, E. F. Schwier, M. G. Garnier, N. Mariotti, C. Didiot, H. Beck, P. Aebi, H. Cercellier, J. Marcus, C. Battaglia, H. Berger, and A. N. Titov, "Temperature-dependent photoemission on 1T–TiSe₂: Interpretation within the exciton condensate phase model," Phys. Rev. B **81**, 155104 (2010).

[77] T. M. Project, "Materials data on MoSe₂ by materials project," (Lawrence Berkeley National Lab. (LBNL), Berkeley, CA, 2020).

[78] H. Shibata, "Negative thermal quenching curves in photoluminescence of solids," Jpn. J. Appl. Phys., Part 1 **37**, 550–553 (1998).

[79] J. Huang, T. B. Hoang, and M. H. Mikkelsen, "Probing the origin of excitonic states in monolayer WSe₂," Sci. Rep. **6**, 22414 (2016).

[80] S. S. Lin, B. G. Chen, W. Xiong, Y. Yang, H. P. He, and J. Luo, "Negative thermal quenching of photoluminescence in zinc oxide nanowire-core/graphene-shell complexes," Opt. Express **20**, A706 (2012).

[81] A. Kogar *et al.*, "Signatures of exciton condensation in a transition metal dichalcogenide," Science **358**, 1314–1317 (2017).

[82] C. Lian, Z. A. Ali, and B. M. Wong, "Charge density wave hampers exciton condensation in 1T-TiSe₂," Phys. Rev. B **100**, 205423 (2019).

[83] D. Van Tuan, B. Scharf, I. Žutić, and H. Dery, "Marrying excitons and plasmons in monolayer transition-metal dichalcogenides," Phys. Rev. X **7**, 041040 (2017).

[84] D. Van Tuan, B. Scharf, Z. Wang, J. Shan, K. F. Mak, I. Žutić, and H. Dery, "Probing many-body interactions in monolayer transition-metal dichalcogenides," Phys. Rev. B **99**, 085301 (2019).

[85] B. Scharf, D. Van Tuan, I. Žutić, and H. Dery, "Dynamical screening in monolayer transition-metal dichalcogenides and its manifestations in the exciton spectrum," J. Phys.: Condens. Matter **31**, 203001 (2019).

[86] D. Van Tuan, B. Scharf, I. Žutić, and H. Dery, "Intervalley plasmons in crystals," arXiv:1901.02567 (2019).

Supporting Information: Charge Density Wave Activated Excitons in TiSe$_2$ - MoSe$_2$ Heterostructures

Jaydeep Joshi,[1,2] Benedikt Scharf,[3] Igor Mazin,[1,2] Sergiy Krylyuk,[4] Daniel J. Campbell,[5] Johnpierre Paglione,[5,6] Albert Davydov,[4,2,5] Igor Žutić,[7] and Patrick M. Vora*[1,2]

[1)]*Department of Physics and Astronomy, George Mason University, Fairfax, Virginia 22030, United States*

[2)]*Quantum Science and Engineering Center, George Mason University, Fairfax, Virginia 22030, United States*

[3)]*Institute for Theoretical Physics and Astrophysics and Würzburg-Dresden Cluster of Excellence ct.qmats, University of Würzburg, Am Hubland, 97074, Würzburg, Germany*

[4)]*Materials Science and Engineering Division, National Institute of Standards and Technology, Gaithersburg, Maryland 20899, United States*

[5)]*Maryland Quantum Materials Center, Department of Physics, University of Maryland, College Park, Maryland 20742, United States*

[6)]*Canadian Institute for Advanced Research, Toronto, Ontario M5G 1Z8, Canada*

[7)]*Department of Physics, University at Buffalo, Buffalo, New York 14260, United States*

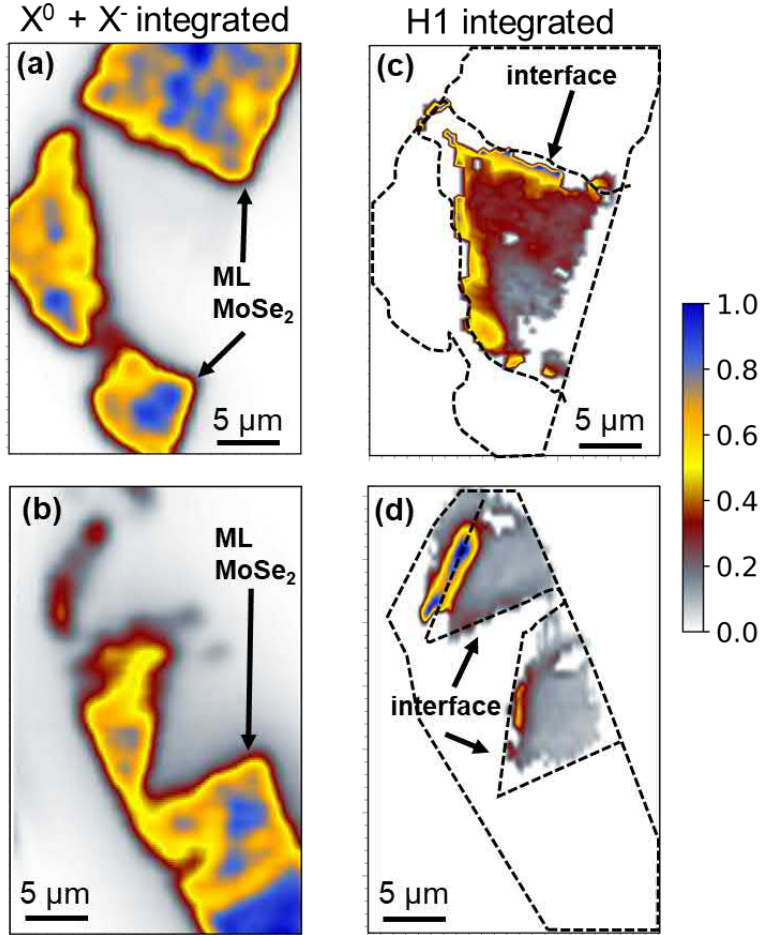# I. S1: PL INTEGRATED INTENSITIES IN SAMPLE 1 AND SAMPLE 2

FIG. S1. Spatially-mapped photoluminescence (PL) integrated intensity of the sum of exciton (X^0) and trion (X^-) peaks (1.6 eV - 1. 66 eV) for (a) Sample 1 and (b) Sample 2. Spatially-mapped PL integrated intensity of the high-energy feature H1 (1.66 - 1.7 eV) for (c) Sample 1 and (d) Sample 2. In case of the X^0 and X^- PL, we see a factor of five reduction pf the integrated intensity at the interface compared to the pristine region. We can see for Sample 1, H1 is present only across the interface, while for Sample 2, H1 is rather prominent along the edges, and weak over the junction. These differences in the spatial intensity of H1 can be attributed to different coupling regimes between the two samples as shown in Fig. 1 of the main manuscript.

Spatially-mapped PL integrated intensities of the total X^0 and X^- emission (panels (a) and (b)) and the H1 emission (panels (c) and (d)) in Sample 1 and Sample 2.

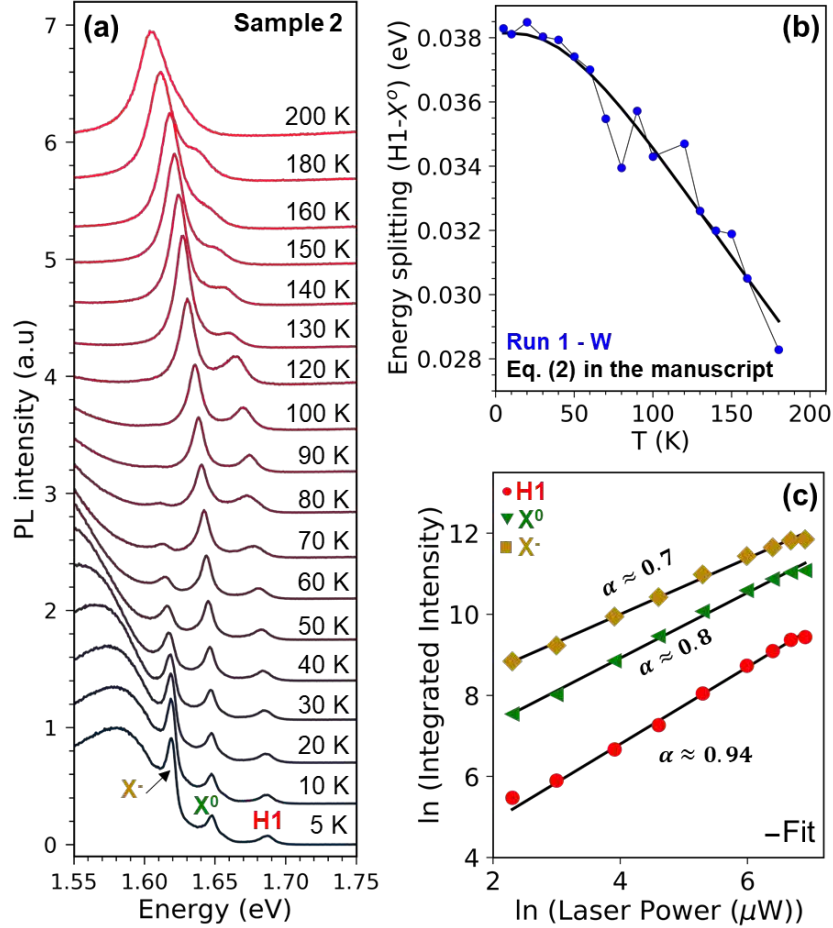## II. S2: TEMPERATURE- AND POWER-DEPENDENT PL IN SAMPLE 2

FIG. S2. (a) Temperature-dependent PL plots taken at the $TiSe_2$ - $MoSe_2$ interface (Sample 2) in the range of 5 K - 200 K. We observe three distinct transitions: X^-, X^0 and H1. (b) Energy of the H1 peak with respect to X^0 showing a BCS type temperature-dependence. The solid black line is fit to an empirical model described by Eq. (2) in the main manuscript. (c) Power-dependent data showing linearity of X^0 peak, where the solid black line is a power-law fit ($I \propto P^\alpha$) with α approaching 1 for H1, while a sublinear behavior of the X^0 and X^- peaks is observed. These results are similar to our observations of Sample 1 discussed in the manuscript.

Temperature and power-dependent measurements on sample 2, showing the CDW dependence of H1 peak. We see similar trends as in Sample 1 discussed in the main manuscript.

III. S3: DENSITY FUNCTIONAL CALCULATIONS OF THE BAND ALIGNMENT

DFT calculations for semiconductors always have to be taken with a grain of salt because of the infamous derivative discontinuity problem affecting the band gap. Furthermore, the large lattice mismatch between the $TiSe_2$ and $MoSe_2$ makes it necessary to use large supercells to restore the lateral periodicity. With these reservations, we have attempted an estimate of the band alignment using a just a $MoSe_2$ - $TiSe_2$ bilayer. One can construct a supercell[1] consisting of 2×2 $TiSe_2$ unit cells and $\sqrt{7} \times \sqrt{29}$ $MoSe_2$ unit cells, rotated by $\approx 36°$ and expanded by $\approx 1.3\%$ (Fig. S3(a)).
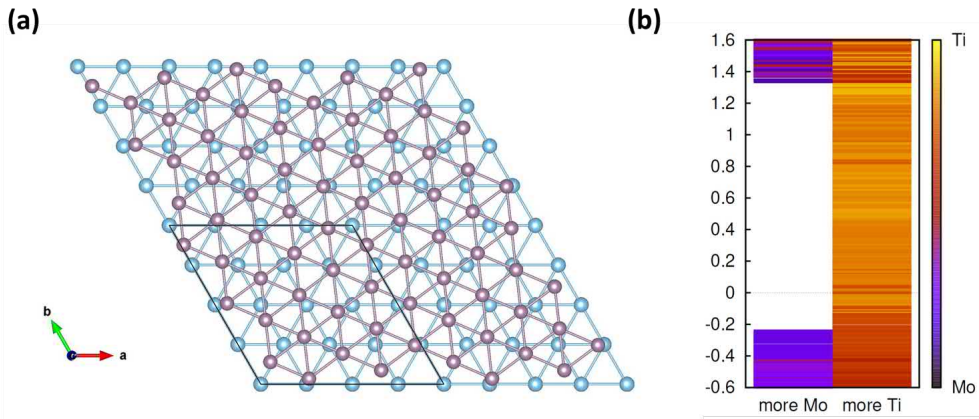

FIG. S3. (a) Supercell including 16 $MoSe_2$ and 19 $TiSe_2$ units. (b) band alignment diagram for the same supercell, based on the projected Ti and Mo characters. The state with more Mo characters are depicted on the left hand side, with more Ti characters on the right hand side.

With this unit cell, we have optimized the internal coordinates and the interlayer distance using the Vienna Ab-initio Simulation Package (VASP)[2] with the PBE-GGA approximation to the exchange correlation potential[3] and PAW pseudo-potentials[4], including the van der Waals correction from Ref. 5. After that, we have listed all one-electron states according to whether their main character is Mo (left on Fig. S3(b)), or Ti (right). Since most states are either predominantly Mo or predominantly Ti, we can clearly see the top of the $MoSe_2$ valence band is about 230 meV below the Fermi level (which is set to zero). As Fig. S3(b) shows, the $TiSe_2$ in this DFT calculations is metallic, as usual in the uncorrected DFT, but opening a small gap around $E = 0$ in Fig. S3(b) will not change the main conclusion.

IV. S4: THEORY OF EXCITON-PLASMON COUPLING

A. General Model

The close proximity of the MoSe$_2$ and TiSe$_2$ layers also allows for the possibility of the MoSe$_2$ excitons to interact with plasmons excited in TiSe$_2$. To treat the interaction between the excitons and plasmons, we employ the methods developed in Ref. 6 for exciton-phonon coupling and in Refs. 7–10 for exciton-intervalley plasmon coupling and adjust them to account for MoSe$_2$ excitons and TiSe$_2$ plasmons instead.

In the following, we consider only one species of (bright) excitons in MoSe$_2$ for simplicity and assume that these excitons originate from electron-hole excitations between a single conduction band and a single valence band. Then the corresponding MoSe$_2$ electrons are described by the Hamiltonian

$$H_{e-h} = \sum_{\boldsymbol{k}} \left[\epsilon_c(\boldsymbol{k})\hat{a}^\dagger_{c,\boldsymbol{k}}\hat{a}_{c,\boldsymbol{k}} + \epsilon_v(\boldsymbol{k})\hat{a}^\dagger_{v,\boldsymbol{k}}\hat{a}_{v,\boldsymbol{k}} \right] + \frac{1}{2}\sum_{\boldsymbol{k}_1\boldsymbol{k}_2\boldsymbol{k}_3\boldsymbol{k}_4} V_{\boldsymbol{k}_1\boldsymbol{k}_2,\boldsymbol{k}_3\boldsymbol{k}_4}\hat{a}^\dagger_{v,\boldsymbol{k}_1}\hat{a}^\dagger_{c,\boldsymbol{k}_2}\hat{a}_{c,\boldsymbol{k}_3}\hat{a}_{v,\boldsymbol{k}_4}, \quad (1)$$

where $\hat{a}^\dagger_{c,\boldsymbol{k}}$ ($\hat{a}_{c,\boldsymbol{k}}$) and $\hat{a}^\dagger_{v,\boldsymbol{k}}$ ($\hat{a}_{v,\boldsymbol{k}}$) are creation (annihilation) operators for electrons in the conduction and valence bands, respectively. Here the relative crystal momentum $\boldsymbol{k}$ is measured from the conduction band edge, $\epsilon_c(\boldsymbol{k})$ and $\epsilon_v(\boldsymbol{k})$ describe the electron dispersions of the conduction and valence bands, and $V_{\boldsymbol{k}_1\boldsymbol{k}_2,\boldsymbol{k}_3\boldsymbol{k}_4}$ is the matrix element of the electron-electron interaction.

Within the Tamm-Dancoff approximation, excitons X with momentum $\boldsymbol{q}$ arising from Eq. (1) are given by $|X,\boldsymbol{q}\rangle = \prod_{\boldsymbol{k}} \mathcal{A}^{X,\boldsymbol{q}}_{vc\boldsymbol{k}}\, \hat{a}^\dagger_{c,\boldsymbol{k}+\boldsymbol{q}}\hat{a}_{v,\boldsymbol{k}} |\text{GS}\rangle$, where $|\text{GS}\rangle$ is the ground state with fully occupied valence bands. The coefficients $\mathcal{A}^{X,\boldsymbol{q}}_{vc\boldsymbol{k}}$ can be determined by diagonalizing an eigenvalue equation corresponding to a Bethe-Salpeter equation[11]. The corresponding free exciton Green function acquires the form[7–9,12,13]

$$G_0(\Omega, \boldsymbol{q}) = \frac{1}{\Omega - E_X(\boldsymbol{q})}, \quad (2)$$

where Ω is a bosonic Matsubara frequency, $\boldsymbol{q}$ the exciton momentum and $E_X(\boldsymbol{q})$ its energy. The energy of the exciton is given by $E_X(\boldsymbol{q}) = E_{X0} + \hbar^2 q^2/2M$, where E_{X0} is the position of the MoSe$_2$ exciton with $\boldsymbol{q} = \boldsymbol{0}$ and the exciton mass $M = m_c + m_v$ consists of the effective masses of the conduction and valence bands from which the exciton is formed.

5

Furthermore, we assume that the conduction-band electrons that participate in the formation of the MoSe$_2$ excitons are coupled to plasmons in the adjacent TiSe$_2$ layer by

$$H_{e-pl} = \sum_{\boldsymbol{q},\boldsymbol{k}} \mathcal{M}_{\boldsymbol{q}} \left(\hat{b}_{-\boldsymbol{q}} + \hat{b}_{\boldsymbol{q}}^\dagger \right) \hat{a}_{c,\boldsymbol{k}-\boldsymbol{q}}^\dagger \hat{a}_{c,\boldsymbol{k}}, \tag{3}$$

where $\hat{a}_{c,\boldsymbol{k}}^\dagger$ and $\hat{a}_{c,\boldsymbol{k}}$ have been defined above in Eq. (1) and $\hat{b}_{\boldsymbol{q}}^\dagger$ and $\hat{b}_{\boldsymbol{q}}$ are creation and annihilation operators for plasmons in TiSe$_2$. The electron-plasmon coupling strength is given by $\mathcal{M}_{\boldsymbol{q}}$ and $\boldsymbol{q}$ denotes the plasmon momentum here. In Eq. (3) we have assumed momentum conservation and only on type of plasmons for simplicity.

The TiSe$_2$ plasmons are described by the free plasmon propagator

$$D(\Omega, \boldsymbol{q}) = \frac{2\hbar\omega_{\boldsymbol{q}}}{\Omega^2 - \hbar^2\omega_{\boldsymbol{q}}^2}, \tag{4}$$

where Ω is again a bosonic Matsubara frequency and $\omega_{\boldsymbol{q}}$ the TiSe$_2$ plasmon dispersion. Exciton-plasmon coupling then leads to a dressed MoSe$_2$ exciton Green function,

$$G(\Omega, \boldsymbol{q}) = \frac{G_0(\Omega, \boldsymbol{q})}{1 - G_0(\Omega, \boldsymbol{q})\Sigma(\Omega, \boldsymbol{q})}. \tag{5}$$

Here the self-energy $\Sigma(\Omega, \boldsymbol{q})$ due to TiSe$_2$ plasmons is given—to lowest order—by

$$
\begin{aligned}
\Sigma(\Omega, \boldsymbol{q}) &= -k_{\mathrm{B}}T \sum_{\boldsymbol{q}',\Omega'} |\mathcal{M}_{\boldsymbol{q}'}|^2 D(\Omega - \Omega', \boldsymbol{q}')G_0(\boldsymbol{q} + \boldsymbol{q}', \Omega') \\
&= -\sum_{\boldsymbol{q}'} |\mathcal{M}_{\boldsymbol{q}'}|^2 \left[\frac{g(E_X(\boldsymbol{q} + \boldsymbol{q}')) - g(\hbar\omega_{\boldsymbol{q}'})}{\Omega + \hbar\omega_{\boldsymbol{q}'} - E_X(\boldsymbol{q}' + \boldsymbol{q})} - \frac{g(E_X(\boldsymbol{q}' + \boldsymbol{q})) - g(-\hbar\omega_{\boldsymbol{q}'})}{\Omega - \hbar\omega_{\boldsymbol{q}'} - E_X(\boldsymbol{q}' + \boldsymbol{q})} \right] \\
&= \sum_{\boldsymbol{q}'} |\mathcal{M}_{\boldsymbol{q}'}|^2 \left[\frac{g(\hbar\omega_{\boldsymbol{q}'}) - g(E_X(\boldsymbol{q} + \boldsymbol{q}'))}{\Omega + \hbar\omega_{\boldsymbol{q}'} - E_X(\boldsymbol{q}' + \boldsymbol{q})} + \frac{g(\hbar\omega_{\boldsymbol{q}'}) + 1 + g(E_X(\boldsymbol{q}' + \boldsymbol{q}))}{\Omega - \hbar\omega_{\boldsymbol{q}'} - E_X(\boldsymbol{q}' + \boldsymbol{q})} \right] \tag{6}
\end{aligned}
$$

with the Boltzmann constant k_{B}, the temperature T, and the Bose-Einstein distribution function

$$g(\epsilon) = \frac{1}{\exp\left[\epsilon/(k_B T)\right] - 1}. \tag{7}$$

The self-energy contribution from Eq. (6) corresponds to the propagation of an exciton which temporarily transitions into a different exciton state by absorbing or emitting a plasmon. In the second step in Eq. (6) we have performed the sum over bosonic Matsubara frequencies and in the third step we have used that $g(-\epsilon) = -1 - g(\epsilon)$. To arrive at Eq. (6), we have assumed that exciton-plasmon coupling arises from electron-plasmon coupling (with the valence-band electrons acting as spectators)[7–9].

Typically, one is mostly interested in excitons with $\boldsymbol{q} = \boldsymbol{0}$ and we consider this case in the following. Then the absorption, which is proportional to the imaginary part of the exciton Green function, is given by

$$\alpha(\omega) \propto -\mathrm{Im}\left[G(\Omega \to \hbar\omega + \imath\Gamma, \boldsymbol{0})\right] \tag{8}$$

after analytical continuation of Ω, where $\hbar\omega$ denotes photon energies and Γ a phenomenological broadening. Likewise, PL can be related to the Green function via[13]

$$\mathcal{L}(\omega) \propto -\mathrm{Im}\left[G(\Omega \to \hbar\omega + \imath\Gamma, \boldsymbol{0})\right] g(\hbar\omega - \mu), \tag{9}$$

where g is again the Bose-Einstein distribution and μ is the quasichemical potential of the electron-hole pairs. We are only interested in the dilute limit, $\mu \ll E_{X0}$, and can therefore approximate Eq. (9) by

$$\mathcal{L}(\omega) \propto -\mathrm{Im}\left[G(\Omega \to \hbar\omega + \imath\Gamma, \boldsymbol{0})\right] g(\hbar\omega) \tag{10}$$

in the following.

B. Simplified Model Used

Since we cannot assume momentum conservation between the MoSe$_2$ excitons and the TiSe$_2$ plasmons, we use a simplified model and assume that $\mathcal{M}$ is momentum-independent. Moreover, we assume that the exciton momentum is completely independent of the plasmon momentum, that is, we use $E_X(\boldsymbol{q})$ instead of $E_X(\boldsymbol{q}+\boldsymbol{q}')$. With these simplifications, Eq. (6) becomes

$$\Sigma(\Omega, \boldsymbol{q} = \boldsymbol{0}) = |\mathcal{M}|^2 \sum_{\boldsymbol{q}'} \left[\frac{g(\hbar\omega_{\boldsymbol{q}'}) - g(E_X(0))}{\Omega + \hbar\omega_{\boldsymbol{q}'} - E_X(0)} + \frac{g(\hbar\omega_{\boldsymbol{q}'}) + 1 + g(E_X(0))}{\Omega - \hbar\omega_{\boldsymbol{q}'} - E_X(0)}\right] \tag{11}$$

for $\boldsymbol{q} = \boldsymbol{0}$.

To further simplify our discussion, we from now on neglect the momentum dependence of the excitons and assume the plasmon does not have a dispersion and has just one plasmon energy $\hbar\omega_{pl}$. Then Eq. (11) becomes

$$\Sigma(\Omega) = |\mathcal{M}|^2 \left[\frac{g(\hbar\omega_{pl}) - g(E_{X0})}{\Omega + \hbar\omega_{pl} - E_{X0}} + \frac{g(\hbar\omega_{pl}) + 1 + g(E_{X0})}{\Omega - \hbar\omega_{pl} - E_{X0}}\right], \tag{12}$$

where E_{X0} is the zero-momentum exciton energy.

Adjusting the dressed exciton Green function given by Eq. (5) to our simplified model yields

$$G(\Omega) = \frac{1}{\Omega - E_{X0} - \Sigma(\Omega)}. \tag{13}$$

It proves instructive to study the poles of the dressed Green function at $T = 0$ more closely. At $T = 0$, the self-energy is simply

$$\Sigma(\Omega) = \frac{|\mathcal{M}|^2}{\Omega - E_{X0} - \hbar\omega_{pl}}, \tag{14}$$

which has a pole at $\Omega = E_{X0} + \hbar\omega_{pl}$. The Green function (in Eq. (13)) then becomes

$$G(\Omega) = \frac{\Omega - E_{X0} - \hbar\omega_{pl}}{(\Omega - E_{X0})(\Omega - E_{X0} - \hbar\omega_{pl}) - |\mathcal{M}|^2}, \tag{15}$$

which has poles at

$$\Omega = E_{X0} + \frac{\hbar\omega_{pl} \pm \sqrt{(\hbar\omega_{pl})^2 + |\mathcal{M}|^2}}{2}. \tag{16}$$

Hence, at low T the dressed exciton Green function exhibits one pole close to the original exciton peak position at $\hbar\omega \approx E_{X0}$ and another one close to $\hbar\omega \approx E_{X0} + \hbar\omega_{pl}$. If the plasmon population $g(\hbar\omega_{pl})$ increases, either by raising T or by otherwise exciting plasmons in the TiSe$_2$ layer, a third peak, which is located in the vicinity of $\hbar\omega \approx E_{X0} - \hbar\omega_{pl}$, arises.

C.   Results

These statements are corroborated by Fig. S4, which shows $-\mathrm{Im}\,[G(\Omega \to \hbar\omega + \imath\Gamma, \mathbf{0})]$ as a function of the photon energy for different exciton-plasmon coupling strengths [Fig. S4(a)] and for different temperatures [Fig. S4(b)]. At low temperatures, one can clearly see that in addition to the exciton peak at $\hbar\omega \approx E_{X0}$, a side peak emerges at photon energies above E_{X0} due to exciton-plasmon coupling. With increasing coupling strength $\mathcal{M}$, more spectral weight is transferred to this side peak, as illustrated by Fig. S4(a). Fig. S4(a), moreover, shows that exciton-plasmon coupling also leads to a renormalization of the position of the exciton, as described by Eq. (16).

Increasing the temperature leads to an increased TiSe$_2$ plasmon population, which in turn results in the appearance of a second side peak due to exciton-plasmon coupling, as can be discerned from Fig. S4(b). This second side peak is located below the exciton
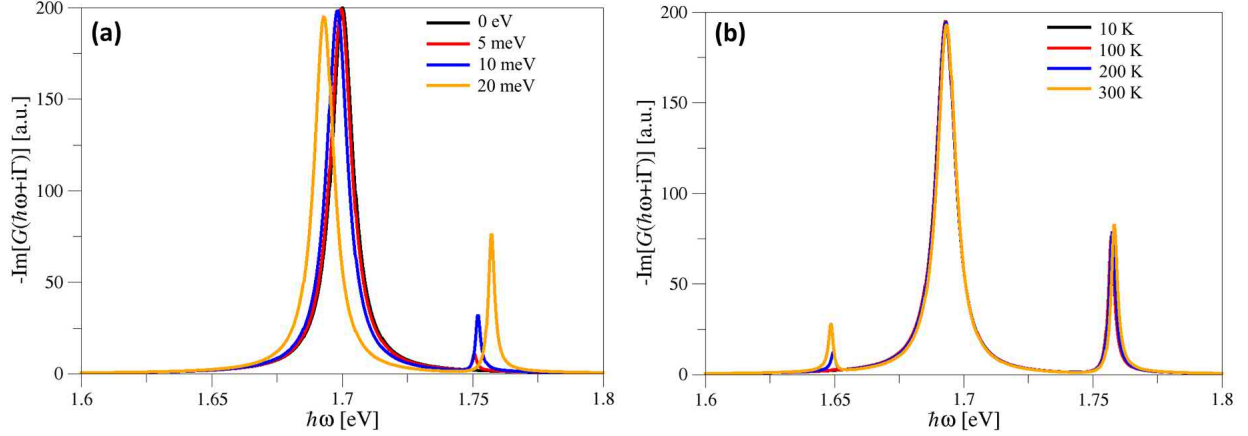
8

FIG. S4. Imaginary part of the dressed exciton Green function computed from Eqs. (12) and (13) as a function of the photon energy $\hbar\omega$ for (a) different exciton-plasmon coupling strengths $\mathcal{M}$ and (b) for different temperatures T. In panel (a) the temperature is fixed at $T = 10$ K and in panel (b) $\mathcal{M} = 20$ meV. In all plots, $E_{X0} = 1.7$ eV, $\hbar\omega_{pl} = 50$ meV, and $\Gamma = 5$ meV. To evaluate $\Sigma(\Omega \rightarrow \hbar\omega + \imath\Gamma_\Sigma)$ a separate broadening of $\Gamma_\Sigma = 1$ meV has been taken.

peak at $\hbar\omega \approx E_{X0}$ and its spectral weight increases with increasing temperature. Since $-\mathrm{Im}\left[G(\Omega \rightarrow \hbar\omega + \imath\Gamma, \mathbf{0})\right]$ enters both the absorption and PL via Eqs. (8) and (9), one can conclude that those also exhibit an additional side peak at $\hbar\omega \approx E_{X0} + \hbar\omega_{pl}$ at low temperatures if the exciton-plasmon coupling is sufficiently strong.

9

REFERENCES

[1] "Courtesy of Madeleine Phillips, NRL,".

[2] G. Kresse and J. Hafner, "*Ab initio* molecular dynamics for liquid metals," Phys. Rev. B **47**, 558–561 (1993).

[3] J. P. Perdew, K. Burke, and M. Ernzerhof, "Generalized gradient approximation made simple," Phys. Rev. Lett. **77**, 3865–3868 (1996).

[4] P. E. Blöchl, "Projector augmented-wave method," Phys. Rev. B **50**, 17953–17979 (1994).

[5] S. Grimme, J. Antony, S. Ehrlich, and H. Krieg, "A consistent and accurate ab initio parametrization of density functional dispersion correction (dft-d) for the 94 elements h-pu," J. Chem. Phys. **132**, 154104 (2010).

[6] G. Antonius and S. G. Louie, "Theory of the Exciton-Phonon Coupling," arXiv:1705.04245 (2017).

[7] D. Van Tuan, B. Scharf, I. Žutić, and H. Dery, "Marrying excitons and plasmons in monolayer transition-metal dichalcogenides," Phys. Rev. X **7**, 041040 (2017).

[8] D. Van Tuan, B. Scharf, Z. Wang, J. Shan, K. F. Mak, I. Žutić, and H. Dery, "Probing many-body interactions in monolayer transition-metal dichalcogenides," Phys. Rev. B **99**, 085301 (2019).

[9] B. Scharf, D. V. Tuan, I. Žutić, and H. Dery, "Dynamical screening in monolayer transition-metal dichalcogenides and its manifestations in the exciton spectrum," J. Phys.: Condens. Matter **31**, 203001 (2019).

[10] D. Van Tuan, B. Scharf, I. Žutić, and H. Dery, "Intervalley plasmons in crystals," arXiv:1901.02567 (2019).

[11] M. Rohlfing and S. G. Louie, "Electron-hole excitations and optical spectra from first principles," Phys. Rev. B **62**, 4927–4944 (2000).

[12] H. Haug and S. Schmitt-Rink, "Electron theory of the optical properties of laser excited semiconductors," Prog. Quant. Electr. **9**, 3 (1984).

[13] S. Schmitt-Rink, C. Ell, and H. Haug, "Many-body effects in the absorption, gain, and luminescence spectra of semiconductor quantum-well structures," Phys. Rev. B **33**, 1183–1189 (1986).